Solar tomography adaptive optics

Deqing Ren,[1,2,3,*] Yongtian Zhu,[2,3] Xi Zhang,[2,3] Jiangpei Dou,[2,3] and Gang Zhao[2,3]

[1]Physics & Astronomy Department, California State University Northridge,
18111 Nordhoff Street, Northridge, California 91330, USA

[2]National Astronomical Observatories/Nanjing Institute of Astronomical Optics & Technology,
Chinese Academy of Sciences, Nanjing 210042, China

[3]Key Laboratory of Astronomical Optics & Technology, Nanjing Institute of Astronomical Optics & Technology,
Chinese Academy of Sciences, Nanjing 210042, China

*Corresponding author: ren.deqing@csun.edu

Conventional solar adaptive optics uses one deformable mirror (DM) and one guide star for wave-front sensing, which seriously limits high-resolution imaging over a large field of view (FOV). Recent progress toward multiconjugate adaptive optics indicates that atmosphere turbulence induced wave-front distortion at different altitudes can be reconstructed by using multiple guide stars. To maximize the performance over a large FOV, we propose a solar tomography adaptive optics (TAO) system that uses tomographic wave-front information and uses one DM. We show that by fully taking advantage of the knowledge of three-dimensional wave-front distribution, a classical solar adaptive optics with one DM can provide an extra performance gain for high-resolution imaging over a large FOV in the near infrared. The TAO will allow existing one-deformable-mirror solar adaptive optics to deliver better performance over a large FOV for high-resolution magnetic field investigation, where solar activities occur in a two-dimensional field up to 60″, and where the near infrared is superior to the visible in terms of magnetic field sensitivity.   © 2014 Optical Society of America

OCIS codes: (110.1080) Active or adaptive optics; (110.0115) Imaging through turbulent media.
http://dx.doi.org/10.1364/AO.53.001683

1. Introduction

The study of two-dimensional solar fine structures requires high-resolution imaging over a large field of view (FOV). One of the future developments of the solar adaptive optics is multiconjugate adaptive optics (MCAO). For a MCAO system, several deformable mirrors (DMs), each conjugated to a different height above the telescope aperture, are used so that the atmospheric turbulences at different altitudes can be corrected for high-resolution imaging over a large FOV [1–5]. Recently, using five laser guide stars, the Gemini MCAO System (GeMS) successfully demonstrated the feasibility to deliver high-resolution imaging over a large FOV over 60″ [6]. Although MCAO is a promising technique for atmospheric turbulence correction, nighttime MCAO is difficult to perform, since multiple laser guide stars are needed for tomographic wave-front sensing. To accurately reconstruct the turbulence profile at different altitudes/heights for a MCAO system, generally at least three to five laser guide stars are needed. The sun is a natural target for extended object wave-front sensing, and any number of "guide stars" could be made from a two-dimensional structure image.

Two different MCAO techniques exist, and both deploy multiple DMs conjugated on different heights. One is the layer-oriented approach [7]. The layer-oriented MCAO was initially introduced for nighttime observations, in which each wave-front sensor

(WFS) and its associated DM are conjugated to a specific height above the telescope; the other is the star-oriented MCAO, in which a number of guide stars are used by several WFSs, and the wave-front profile at different heights can be reconstructed via the tomography approach [3] and the reconstructed global wave-front information can be used to control DMs. Until now, solar layer-oriented MCAO has not yet been demonstrated in practice. The solar ground-layer AO (GLAO) can be viewed as a layer-oriented MCAO system that deploys one DM only. Rimmele *et al.* [8] tested a solar GLAO correction with the NSO Dunn Solar Telescope: they used a WFS conjugated to the ground and averaged the wave-front distortions over a $42'' \times 42''$ FOV, and the wave-front data were used to control the DM conjugated to the ground. The experiment was, however, unsuccessful. Kellerer [9] further pointed out that fields of several arc minutes in diameter are required to attenuate the signal from layers above 2–3 km altitude, which excludes the solar layer-oriented approach for GLAO systems, at least with current technology.

Current solar MCAO experiments exclusively use the star-oriented approach. The height distribution of the turbulence profile can be determined via tomographic wave-front sensing. To verify the MCAO concept for solar high-resolution imaging, two prototypes are being developed: one for the 0.7 m Dunn Solar Telescope at the NSO [10], and the other with the VTT and GREGOR [11].

A sunspot or active region may extend up to ∼60″. Flares can occur unannounced anywhere in the extended FOV. Flare trigger mechanisms operate rapidly and on the smallest spatial scales, and their location within the FOV is difficult to predict. Diffraction-limited imaging over a FOV of ∼60″ is required in these cases [12]. To achieve such a challenging goal, several DMs are needed for a solar MCAO system. For example, the MCAO for the planned 4 m European Solar Telescope (EST) requires us to achieve a Strehl ratio of $S = 0.3$ for the $r_0 = 7$ cm seeing over a FOV of 60″ in visible wavelengths. To achieve such a Strehl ratio over the large FOV, the design uses five DMs and 7–19 guide stars [13].

Due to the complexity of the MCAO, there is no solar MCAO in routine operation until now. In this publication, we propose a simple solar adaptive optics system called tomography adaptive optics (TAO), which deploys one DM only, and it fully takes advantage of the three-dimensional wave-front information derived from multiple guide stars, so that the best DM profile can be found to correct the turbulence induced wave-front over a large FOV. We show that our star-oriented TAO can deliver good performance in the near-infrared (NIR) J and H bands, and can be used in the NIR to replace MCAO that requires several DMs. Our TAO is different from the solar GLAO, in that a GLAO system cannot reconstruct the three-dimensional wave-fronts, and therefore its performance may be limited. By fully

taking advantage of the knowledge of the three-dimensional turbulence distribution reconstructed by the WFS, the DM in our TAO can be conjugated to a best-conjugated height, which will provide a further performance improvement. We noted that the concept of laser tomographic AO (LTAO) was proposed for nighttime astronomy [14], which requires the use of both laser and NGSs, and it has not involved the best-conjugated height. In Section 2, we discuss how to calculate the three-dimensional seeing profile that is critical for the TAO performance estimation. The numerical simulations of our TAO performance in the visible and NIR are presented in Section 3. Further discussions are presented in Section 4. We achieve our conclusions in Section 5.

2. Three-Dimensional Turbulence Profiles

To reconstruct the seeing profile at different heights, a number of guide stars are needed. At present, a detailed three-dimension solar turbulence profile is not available, and very little work has been published for characterizing the profile as a function of height. Because of the lack of seeing profile data, current solar MCAO simulations [13] use nighttime seeing data to estimate the MCAO performance [15], which is not acceptable for the TAO simulation, where only one DM is used and is thus very sensitive to the seeing profile distribution. Measurements of scintillation of sunlight with a linear array of detectors have been shown to be sensitive to the height distribution of turbulence contributions [16–18]. However, because of the integration of contributions to scintillation over the large solid angle subtended by the solar disk, an array of detectors with fairly large baseline is needed to achieve sensitivity up to a height of only 500 m [17]. To measure the three-dimensional solar turbulence profiles, Scharmer and van Werkhoven [19] proposed a technique called S-DIMM+. This system, however, has not been used in practice for site survey to generate a seeing profile that can be used quantitatively for solar MCAO performance simulations. The S–DIMM+ was recently used by Kellerer *et al.* [20] to measure the turbulence profile at the BBSO. Unfortunately, the data they collected can only be used statistically to construct four layers of the turbulence distribution [21], which cannot yield accurate results when applied for the TAO simulations.

A general equation that can statistically describe the turbulence profile of a site will be very useful for the TAO as well as MCAO performance simulations. To calculate the turbulence profiles of different sites with different seeing conditions, we use the equation recommended by the team of ATST site survey [22]. That is, the overall solar turbulence profile can be approximated as a sum of a Hufnagel–Valley and an extra term that accounts for the daytime boundary layer. For the turbulence at the height h above the telescope aperture, the so-called Hufnagel–Valley boundary (HVB) model can be

used to calculate the turbulence profile of a solar site [22]:

$$C_n^2(h) = C_{n\text{HV}}^2(h) + A_B \exp(-h/h_0), \qquad (1)$$

where the first part on the right of the equation is the Hufnagel–Valley model that is typically used to calculate the nighttime turbulence profile, and the second part indicates the extra turbulence induced by the daytime ground boundary layer. A_B is the boundary amplitude, and h_o is the boundary scale height. The well-known Hufnagel–Valley model is expressed as

$$C_{n\text{HV}}^2(h) = A_{\text{HV}}\left[2.2 \times 10^{-23}\left(\frac{h+z}{1000}\right)^{10} \exp\left(-\frac{h+z}{1000}\right) \right.$$
$$\left. + 10^{-16} \exp\left(-\frac{h+z}{1500}\right)\right], \qquad (2)$$

where A_{HV} is the amplitude, and z is the site altitude above sea level.

The Fried parameter [23] is used to quantity the seeing condition, and is associated with the turbulence profile C_n^2 as

$$r_0 = \left(0.423\left(\frac{2\pi}{\lambda}\right)^2 (\cos\phi)^{-1} \int C_n^2(h)\mathrm{d}h\right)^{-3/5}, \qquad (3)$$

where λ is the wavelength and ϕ is the zenith angle. For simplification, we assume $\phi = 0°$. That is, the evaluation is done along the zenith direction. ATST site survey measured the seeing Fried parameter of six locations, including lake, island, and continental sites, of which are La Palma (Canary Islands), Sacramento Peak (New Mexico), BBSO (California), and Haleakala (Hawaii) [24]. All the sites have an annual-average seeing around $r_0 = 7.0$ cm. At a site, seeing conditions are variable over the year and they are in general better in summer and worse in winner. For example, while the BBSO delivers a seeing $r_0 = 5.5$ cm with an isoplanatic angle of 2″ in winter, in the summer the seeing is $r_0 = 9.1$ cm with an isoplanatic angle of 6″ at the 0.55 μm wavelength [20], which indicates that the BBSO has an annual-average seeing $r_0 \approx 7.0$ cm and an annual-average isoplanatic angle of 4″. The BBSO experience can be summarized as follows: most of the turbulences are concentrated on four layers, the ground layer (0–500 m), the extended ground layer (1–2 km), the boundary layer (3–7 km), and the tropopause (≥8 km). The distributions of the Fried parameter for the summer (winter) are 12 ± 4 (8 ± 1) cm, 23 ± 8 (13 ± 2) cm, 32 ± 11 (16 ± 2) cm, and 70 ± 28 (32 ± 5) cm for the ground layer r_1, extended ground layer r_2, boundary layer r_3, and tropopause r_3, respectively. This yields an annual-average Fried parameter distribution of 10 ± 2.5 cm, 18 ± 5 cm, 24 ± 6.5 cm, and 51 ± 15 cm for the ground layer r_1, extended ground layer r_2, boundary layer r_3, and tropopause r_3, respectively.

A crucial parameter for the turbulence calculation is the isoplanatic angle, which can be used to characterize the distribution of the turbulence profile. For a fixed seeing parameter r_0, a large isoplanatic angle indicates that more turbulence is concentrated on the ground with a small height h. In the extreme case, if all turbulence is located on the ground exactly on the telescope aperture, one has an infinite isoplanatic angle. According to Roddier [25], for a discrete seeing distribution, the isoplanatic angle can be calculated as

$$\theta_0 = 0.31\left(\sum_i \frac{h_i^{5/3}}{r_0(h_i)^{5/3}}\right)^{-3/5}. \qquad (4)$$

Since the BBSO seeing test is the only site test that delivers the Fried parameter r_0, isoplanatic angle, and limited seeing profile (four layers), and the average seeing Fried parameter r_0 is exactly consistent with the ATST site survey [22], in this paper we will use the BBSO data to reconstruct our 10-layer seeing profile from Eq. (1) for our TAO simulations. The BBSO seeing test delivers an annual-average seeing $r_0 = 7$ cm and an average isoplanatic angle of 4″, respectively. The ground layer (0–500 m) has a Fried parameter $r_1 = 12 \pm 4$ mm. Since mountain sites such as the Sacramento Peak and BBSO typically have an altitude of 2000–3000 m, the altitude z in Eq. (2) is assumed to be 3000 m in our numerical simulation. Based on Eqs. (3) and (4), we can solve for the three unknown parameters A_{HV}, A_B, and h_0. Note that Eq. (3) can be split into two individual equations: one for the overall Fried parameter r_0 and the other for the ground-layer seeing r_1. The three equations yield $A_{\text{HV}} = 0.245$, $A_B = 1.9203 \times 10^{-15}$ and $h_0 = 640$ m. Here, we assume that the turbulence profile is discrete and consists of 10 layers, which is good enough for our one-DM simulations, in which the WFS only needs to reconstruct an equivalent layer for DM correction on a specific height (i.e., on ground or best-conjugated height, respectively; see next section for details). From Eq. (3), we can also calculate the discrete seeing parameter $r_0(h)$ at different height h at the average seeing condition, with the results listed in Table 1, in which the overall Fried parameter r_0 is equal to 7.0 cm and the isoplanatic angle is equal to 4″ at the 0.55 μm wavelength. The above approach allows the seeing profile listed in Table 1 to exactly match the Fried parameter r_0, the isoplanatic angle θ_0, and the ground layer r_1. In fact, it also matches the extended ground layer very well. For example, at the extended ground layer the Fried parameter r_2 at the average seeing condition calculated from the Table 1 seeing profile is 23 cm, which falls in the BBSO's site measurement data of 18 ± 5 cm.

In a similar way, we also calculate the seeing profile at the bad seeing condition in the winter (with $r_0 = 5.5$ cm, isoplanatic angle of 2″, and the ground-layer Fried parameter $r_1 = 8 \pm 1$ mm), and

Table 1. Discrete Seeing Parameter $r_0(h)$ at Different Heights Above the Ground, at Average, Good, and Bad Seeing Conditions, Respectively

Height (m)	200	700	1500	2500	4000	6000	8000	10,000	12,000	14,000
r_o (cm, average seeing)	11	14	21	53	104	190	201	245	342	533
r_o (cm, good seeing)	13	23	56	244	243	201	202	243	342	533
r_o (cm, bad seeing)	8	13	25	79	80	68	68	83	116	180

at the good seeing condition in the summer $= 9.1$ cm (with $r_0 = 9.1$ cm, isoplanatic angle of 6″, and the ground-layer Fried parameter $r_1 = 12 \pm 4$ mm), with the results listed in Table 1 also. These 10-discrete-layer seeing profiles exactly match the Fried parameter r_0, the isoplanatic angle θ_0, and the ground-layer Fried parameter r_1; they also well match the extended ground layer r_1. For the summer (winter) seeing condition, our discrete seeing profile delivers an extended ground layer of $r_1 = 23$ (12) cm, which perfectly matches the BBSO site measured data.

The constraints for the overall seeing parameter, the isoplanatic angle, and the ground-layer seeing are crucial for the calculation of the turbulence profile that may dramatically affect the results of TAO numerical simulation. Our simulations indicated that without these constraints, correct performance evaluations cannot be guaranteed. Tyson stated that a HVB model can be used to calculate the day turbulence profile of any site, if the two parameters of the overall seeing parameter and isoplanatic angle are known or constrained [26,27]. However, Tyson's HVB seeing profile model has not included the boundary scale height factor h_0, and cannot accurately match the ground seeing profile of actual site test data, which makes the simulations less reliable.

3. Performance Simulation

A. Tomography Algorithm

For a conventional adaptive optics (CAO) system, only one guide star and one DM are used, and the correction of the CAO is efficient only in a small FOV, which is limited by the isoplanatic angle. In recent years, MCAO has been used for wide-field correction. For a MCAO system, wide-field atmospheric turbulence compensation is accomplished by means of multiple DMs that apply phase/wave-front adjustments in two or more planes optically conjugate to the distinct ranges along the propagation path. The information to drive these DMs is obtained from WFS measurements of multiple guide stars via a tomographic wave-front reconstruction algorithm [28].

Since the minimization of the residual phase variance maximizes the image quality in the considered direction, the minimum-mean-square-error (MMSE) estimator that minimizes the mean residual phase variance of the guide stars in the FOV of interest is widely used in MCAO performance estimations [29,30]. As described by Fusco et al. [30], there is a link between the MMSE approach and the tomographic reconstruction of the turbulence volume, and they show that the MMSE approach consists of a full tomographic reconstruction of the turbulence volume followed by a projection onto the DMs accounting for the considered FOV of interest.

One of the key issues for the MCAO is the tomographic wave-front reconstruction [30,31]. Ragazzoni et al. [3] analytically demonstrated that the tomographic wave-front can be reconstructed by using multiple guide stars via the so-called modal tomography approach. DMs conjugated on appreciated altitudes can then be used to correct the wave-front retrieved from these guides stars. In our recent numerical simulations [32], the modal tomography approach is adopted to implement tomographic wave-front reconstruction, which confirmed that the tomographic wave-front can be reconstructed reliably by using multiple guide stars. Our simulation results also showed that six guide stars are required for an accurate wave-front reconstruction in the case of three equivalent turbulence layers, and only three guide stars are needed in the case of two equivalent layers. More advanced theories were developed by Johnston and Welsh [2] and Ellerbroek [33], and, further, by Fusco et al. [34]. In these studies, the statistics of the tomographic wave-front were taken into account. They estimate the wave-front distribution in a few equivalent layers, and these layers are then assumed to be corrected by the corresponding number of DMs. In the case in which the atmosphere is composed of a very large number of turbulent layers, only a few guide stars are needed for the MCAO wave-front correction. Femenía and Devaney [35] demonstrated that using three natural guide stars (NGSs), a 2-DM MCAO system can deliver good performance over a FOV up to 60″ in diameter in the NIR K band.

In addition to in the spatial domain, MCAO performance estimations based on minimum residual phase variance can also be made in Fourier domain [29,36]. The maximum Strehl ratio of the corrected starlight image is achieved by minimizing the residual phase variance, and the residual phase variance is minimized if each of the Fourier components in its power spectrum is minimized [36,31]. This approach typically neglects aperture edge effects [37]. However, it enables rapid analysis of MCAO performance, and is sufficiently accurate for many applications, including the TAO preformation simulations in the NIR.

The above discussions regarding MCAO can also be applied to our TAO, except only one DM is used. In this case, tomographic wave-front information can be measured or reconstructed from multiple guide stars by a Shack–Hartmann (S-H) WFS. The

reconstructed tomographic wave-front information is used to control the DM optimized for wave-front corrections over a relatively large FOV, which is based on finding the minimum residual phase variance in the FOV of interest. This is different from the CAO, in which only a guide star is used, and it cannot reconstruct the tomographic wave-fronts and thus cannot be optimized for a high-resolution imaging over a large FOV.

B. Simulation Software

Five well-recognized simulation codes exist, which can be used to analyze our TAO performance. The PAOLA (38), an analytic modeling code, was developed at the National Research Council of Canada's Herzberg Institute of Astrophysics (NRC-HIA) and is now used by many research groups. CIBOLA (Covariance—Including Basic Option for Linear Analysis) [38], a MATLAB-based simulation code, is also an analytical modeling tool that combines and extends features of PAOLA and prior analytical models for tomographic wave-front reconstruction and MCAO. The Arizona Analytic Code, an IDL-based analytic GLAO simulation tool, was developed by Tokovinin [39]. The Arizona Monte Carlo Simulation Code is a Monte Carlo code and was developed at the University of Arizona [40]. The Durham AO simulation platform [41] is also a Monte Carlo code, and was developed at Durham University (UK). These codes were thoroughly tested and compared to one another to ensure a high degree of confidence in the results [37]. In general, the two Monte Carlo codes generally predict somewhat worse performance than the three analytic codes, presumably because of the inclusion in the Monte Carlo simulations of a great range of physical effects, but their simulation results are in excellent agreement [37].

The software we used for the TAO simulation is the CIBOLA, which is written by Dr. Ellerbroek, and is a software package available from the Center for Adaptive Optics (http://cfao.ucolick.org/). CIBOLA is a code for relatively rapid MCAO modeling using linear system methods in the spatial-frequency domain, with details discussed by Ellerbroek [38,42]. The software we used optimizes for the minimum of the mean residual phase variance, which is a function of DM actuator command vector a, and is given by

$$\sigma^2(a) = \arg \ \min\{x^T[W_x - C_{ax}^T W_a^{-1} C_{ax}]x\}, \quad (5)$$

where $W_a = H_a^T W_\phi H_a$, $C_{ax} = H_a^T W_\phi H_x$, and $W_x = H_x^T W_\phi H_x$. While W_ϕ is a symmetric, semi-positive-definite matrix that defines a norm on the vector space of phase space, H_x and H_a are the influence matrices that describe the impact of phase disturbance x and DM actuator command a on the output wave-front $\phi(a)$. To speed up the MCAO performance simulation process, Ellerbroek [42] used the spatial-frequency domain approach that is relatively computationally efficient but still account for many of the

interactions between the fundamental error sources (such as the WFS and DM sampling errors) in the MCAO, with enough accuracy. The MCAO performance can be evaluated in terms of the Strehl ratio, residual wave-front error, and point spread function (PSF). The spatial-frequency domain performance of the CIBOLA was intensively compared with the traditional spatial domain approach. Performance estimates for MCAO systems may be obtained in 1–2 orders of magnitude less time than needed when detailed simulations or analytical models in the spatial domain are used, with a relative discrepancy of ~5% for typical sample problems [42]. CIBOLA was also used for the MCAO performance evaluation for the future 4 m EST [13].

Nighttime adaptive optics uses a point-source guide star for wave-front sensing. Solar wave-front sensing uses a S-H WFS. The wave-front gradient or slope vector at each subaperture of the lenslet array is solved by the cross-correction calculation of a two-dimensional pattern over a FOV. For the TAO, each subfield with a size around 8″ × 8″ can be viewed as a guide star. That is, it is considered as a point-source star, so that we can use the CIBOLA for the solar TAO simulations. At average seeing, the isoplanatic angle is 4″ in the 0.55 μm. The isoplanatic angle is wavelength scalable, and it is 11″ and 15″ in the J and H bands, respectively. Therefore, the finite size of the solar guide star is negligible and can be viewed as a point source at least in the NIR, since the size of the subfield falls in the isoplanatic angle.

C. Performance at Average Seeing Condition

A CAO system deploys one DM and only measures the wave-front from one "guide star"; thus it cannot reconstruct the three-dimensional wave-front profile and cannot find the best DM shape to correct the tomographic wave-fronts over a large FOV. The tomographic wave-fronts can be reconstructed by using multiple guide stars [3], which can be done by using a S-H WFS and was verified by our numerical simulation [32]. Based on the turbulence profile from Table 1, we will be able to simulate the TAO performance, in which the tomographic wave-fronts are measured by a WFS by using several guide stars, and the measured wave-fronts are fed to a DM for wave-front correction.

The telescope we use for the performance simulation has an aperture size of 1.6 m, which represents the current largest operational solar telescope, such as the McMP at Kitt Peak and the NST at BBSO. We assume that a S-H WFS with 7 cm subaperture projected on the telescope aperture is used for wave-front sensing in the 0.55 μm visible, which exactly matches the average seeing parameter r_0. Increasing the subaperture number can reduce the wave-front sampling error. But this will not be practical, since a smaller subaperture may not be able to resolve fine solar granule structures for wave-front sensing. The DM also has an actuator space of 7 cm projected on the telescope aperture, which matches the WFS and
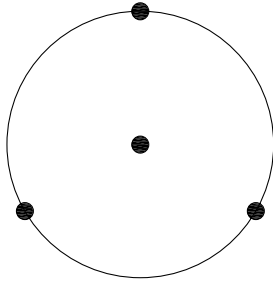
Fig. 1. Asterism of the four guide stars in the OFOV.

will have a small DM fitting error for the correction of turbulence induced wave-front distortion. We also assume that the TAO correction frequency is fast enough so that the correction delay is negligible. Since there are enough photons for solar wave-front sensing and a low-noise camera is available, we further assume both photon and read-out noises are excluded in the simulation. To fully sample a FOV, four guide stars are used, and they are distributed in an optimized field of view (OFOV), in which one guide star is located on the center of the OFOV and the remaining are uniformly located, as shown in Fig. 1. This arrangement ensures good performance for both the on-axis as well as the off-axis positions in the field. In the following subsections, we will simulate the TAO performance in the visible as well as the NIR J and H bands, at the average seeing condition using the seeing data from Table 1.

1. Optimization for the Visible

Diffraction-limited imaging in the visible can answer critical questions for solar astrophysics. For example, $H\alpha$ and Ca II 854.2 nm spectral lines can be used for spectroscopic observations of the solar chromosphere, which will address important questions regarding the dynamics of the quiet inter-network chromosphere and solar flares [43–45].

Using the software CIBOLA, we can evaluate the performance of the TAO in terms of the Strehl ratio (SR). The goal is to find the best performance over the OFOV, which is done by minimizing the residual phase variance from the four guide stars.

Table 2 lists results of the numerical simulation at the 0.55 µm visible wavelength. The DM is optically conjugated on the telescope aperture, and has a zero conjugated height. The SR is calculated as an annulus average value around an imaging FOV up to 60″ in diameter. For comparison, we also provide the SR of the CAO that uses only one guide star and has a zero OFOV, with best SR at the on-axis field position

(i.e., without isoplanatic error). Because of the finite number of wave-front subapertures and DM actuators, the CAO delivers a SR of 0.812 for the on-axis point image. We also evaluate the TAO for the 30″ and 60″ OFOVs, respectively.

Please note the difference between the OFOV and the imaging FOV. The OFOV is defined as the FOV for wave-front sensing and is the field that needs to be optimized, while the imaging FOV is simply a field used to show the imaging performance, and it can be any size. In the visible simulation, the imaging FOVs have a maximum size up to 60″. From the simulation result, it is clear that the TAO with the 30″ OFOV delivers a better SR for off-axis field position than that of the CAO with zero OFOV, at a cost with a lower SR of 0.152 for the on-axis position. The 30″ OFOV delivers a poor performance over the entire OFOV with a SR between 0.152 and 0.022. Of course, its performance is further worse over the entire 60″ imaging FOV. The 60″ OFOV delivers an unacceptable performance with a SR lower than 0.031 over the entire imaging FOV, and should be avoided in the visible wavelengths, where the residual wave-front error is still too large for high-resolution imaging and the gain for the off-axis FOV is very limited. This may explain why current solar GLAO systems with a relatively large wave-front sensing FOV deliver poor performance. Surprisingly, the CAO with a 0″ OFOV delivers a well-balanced SR in the imaging FOV for the on-axis as well as the off-axis positions.

In a summary of the simulation in the visible, wave-front sensing with a small FOV is, in general, superior to that with a large FOV, and a large wave-front sensing FOV should be avoided. In a separate study, Kellerer [6] concluded that current technology excludes the solar GLAO. Our simulation further confirmed that the residual wave-front error induced by high-altitude turbulence is still too large in the visible, which results in a low SR, and which makes any one-DM system impossible to optimize over a large FOV.

2. Optimization for the Near-Infrared J and H Bands

Solar activities are dominated by magnetic fields, and high-resolution imaging in the NIR J and H bands plays a critical role for the investigation of the weak magnetic field. While work using visible spectral lines tends to find kG fields [46,47], observational studies based on the infrared spectral lines can find the magnetic field strength below 1 kG [48,49].

Table 2. Strehl Ratios with Different OFOVs at 0.55 µm Wavelength[a]

Imaging FOV	0″	6″	12″	18″	24″	30″	36″	42″	48″	54″	60″
SR: CAO	0.812	0.326	0.076	0.025	0.013	0.009	0.007	0.006	0.005	0.005	0.004
SR: 30″ OFOV	0.152	0.129	0.091	0.056	0.034	0.022	0.015	0.012	0.009	0.008	0.007
SR: 60″ OFOV	0.031	0.029	0.026	0.023	0.020	0.018	0.016	0.014	0.013	0.011	0.010

[a]Four guide stars are used. Both the OFOV and FOV are defined in diameter.

Table 3. Strehl Ratios with Different OFOVs at 1.25 μm Wavelength and Zero Conjugated Height[a]

Imaging FOV	0″	12″	24″	36″	48″	60″	72″	84″	96″	108″	120″
SR: CAO	0.960	0.580	0.290	0.164	0.107	0.077	0.061	0.051	0.045	0.040	0.036
SR: 30″ OFOV	0.711	0.595	0.434	0.286	0.182	0.131	0.100	0.079	0.067	0.057	0.051
SR: 60″ OFOV	0.458	0.423	0.378	0.317	0.241	0.185	0.143	0.111	0.091	0.076	0.066
SR: 120″ OFOV	0.240	0.231	0.225	0.214	0.194	0.176	0.158	0.138	0.122	0.105	0.093

[a]Four guide stars are used. Both the OFOV and FOV are defined in diameter.

The best-known advantage of the infrared is its great sensitivity to magnetic field observations. This is because the Zeeman splitting $\Delta\lambda_B$, of a magnetically sensitive spectral line, is proportional to $\lambda^2 g_{eff}$, where g_{eff} is the effective Landé factor of the transition. Recently, Ramsauer *et al.* [50] undertook an infrared survey and published a large number of potentially useful spectral lines between 1.0 and 1.8 μm.

If we move to wavelengths in the NIR, the TAO will deliver a different picture. First, we evaluate the TAO performance in the 1.25 μm J band. We use CIBOLA to evaluate the same TAO with the same specifications for the visible, except the wavelength is changed to 1.25 μm and the imaging FOV is extended up to 120″. The results of the numerical simulation are shown in Table 3, in which the DM is conjugated on the telescope aperture, i.e., with a zero conjugated height. Comparing Tables 2 and 3, it is clear that Strehl ratios for 1.25 μm increase dramatically, which benefits from the small residual wave-front error and the longer wavelength in the NIR. The CAO that uses only one guide star delivers a Strehl ratio of 0.960, compared to 0.812 in the visible. The Strehl ratio for the CAO drops quickly, on off-axis positions in the imaging FOV. But it still delivers an acceptable performance for an imaging FOV up to 36″ in diameter (with a Strehl ratio of 0.164). Now, the TAO with 30″ OFOV delivers good performance both on-axis and off-axis over a large imaging FOV. The TAO with 60″ OFOV delivers better overall performance over the on-axis and off-axis imaging FOV, and it delivers good performance over an imaging FOV up to ~60″ (with a Strehl ratio between 0.458 and 0.185). Continuously increasing the

OFOV does not help much. At 120″ OFOV, the on-axis performance drops dramatically, while the off-axis Strehl ratio does not have very much improvement. Obviously, the 60″ FOV is a good choice for the TAO wave-front sensing.

The performance of the TAO can be further improved by moving the DM to a best-conjugated height, where most turbulence is located and can be effectively corrected by the DM. With knowledge of the global seeing profile, we are able to find the best-conjugated height, which is done by shifting the DM's conjugated height and evaluating the TAO performance accordingly at each height. Figure 2 shows the numerical simulation result for the on-axis field Strehl ratio as a function of DM conjugated height for the 60″ OFOV. From this plot, it was found that the best-conjugated height is located at 1100 m, with 100 m sampling step accuracy. The Strehl ratio in any position over the entire 60″ OFOV is also improved in the best-conjuagted height (see Tables 3 and 4 for comparison). However, the on-axis Strehl ratio has the most significant change and is used to find the best-conjugated height.

Table 4 and Fig. 3 show the results of the numerical simulation for the 1.25 μm NIR, with the DM conjugated to the 1100 m best height. For comparison, the CAO with zero OFOV and zero DM conjugated height is still listed in the table. Compared with the CAO, the TAO with a large OFOV received a bigger gain, and delivers excellent performance for an imaging FOV up to ~60″. Now, the TAO with the 120″ OFOV also delivers good performance over the entire 72″ imaging FOV (with 0.211 Strehl ratio on the 72″ imaging FOV). The TAOs with 30″, 60″,
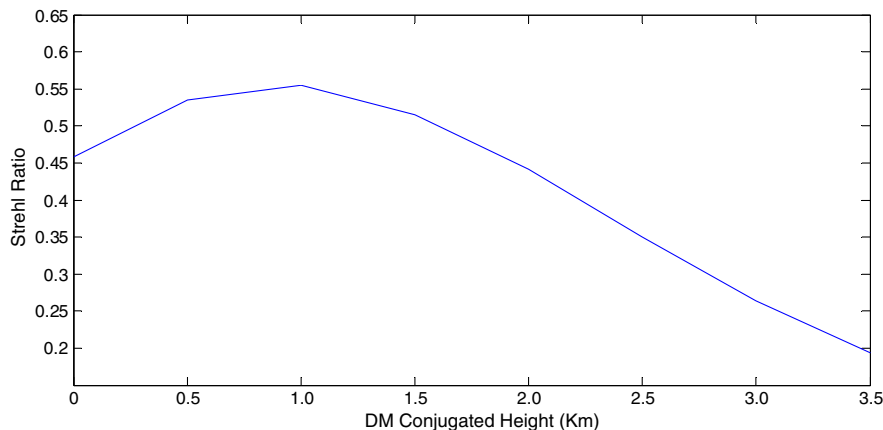
Fig. 2. Strehl ratio as a function of DM conjugated height for the 60″ OFOV. The best-conjugated height is found to be 1.0 km with 0.1 km sampling steps.

Table 4. Strehl Ratios with Different OFOVs at 1.25 μm Wavelength and 1000 m Conjugated Height[a]

Imaging FOV	0″	12″	24″	36″	48″	60″	72″	84″	96″	108″	120″
SR: CAO	0.960	0.580	0.290	0.164	0.107	0.077	0.061	0.051	0.045	0.040	0.036
SR: 30″ OFOV	0.776	0.664	0.514	0.369	0.249	0.180	0.137	0.107	0.087	0.073	0.061
SR: 60″ OFOV	0.555	0.515	0.465	0.403	0.315	0.245	0.191	0.148	0.118	0.096	0.079
SR: 120″ OFOV	0.332	0.321	0.309	0.295	0.266	0.239	0.211	0.181	0.156	0.132	0.112

[a]Four guide stars are used.
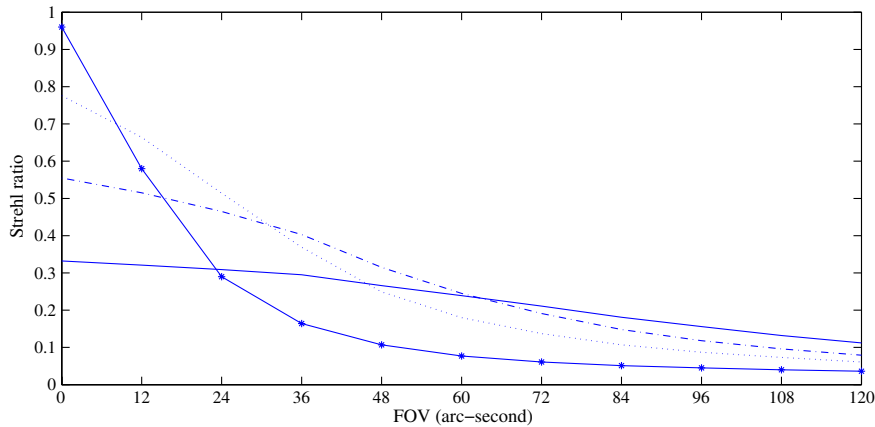
Fig. 3. Strehl ratios with different OFOVs with DM conjugated on 1.0 km height at 1.25 μm NIR. The solid line with star markers represents the CAO; dotted line, optimized for 30″ OFOV; dash dotted line, optimized for 60″ OFOV; solid line without marker, optimized for 120″ FOV.

and 120″ OFOVs all receive a significant Strehl ratio gain both on-axis and off-axis over a large FOV. Again, the 60″ OFOV is a good choice for the TAO wave-front sensing.

The best DM conjugated height can also be calculated analytically with the mean turbulence height H, in the first order for a quick estimation. When there is a single layer of turbulence, H is the height of that layer. For a turbulence profile $C_n^2(h)$, the mean turbulence height can be calculated as [51]

$$H = \left(\frac{\int \mathrm{d}h C_n^2(h) h^{5/3}}{\int \mathrm{d}h C_n^2(h)} \right)^{3/5}, \qquad (6)$$

which leads to the relation

$$\theta_0 = 0.314 (\cos \phi) r_0 / H, \qquad (7)$$

where the zenith angle ϕ is assumed to be zero. For $\theta_0 = 4''$ and $r_0 = 7$ cm (at 0.55 μm), a mean turbulence height of $H = 1128$ m is yielded, which is in good agreement with the 1000 m from the numerical simulation.

Although the best-conjugated height can be calculated using Eq. (6) or Eq. (7), the conjugated height found with the numerical simulation is a better solution. This is because a DM cannot effectively correct the turbulence layers that are far away from the DM conjugated altitude. Therefore, in the rest of this article, we will only use the numerical simulation to find the best-conjugated height.

H band imaging is also important for solar NIR magnetic investigation. Table 5 shows the results of the numerical simulation for the 1.65 μm wavelength, with the DM conjugated on the telescope aperture with zero height. Now, the TAOs with OFOVs from 30″ to 120″ all deliver good performance over the entire imaging FOV up to 60″. The 60″ OFOV is still best for the wave-front sensing, since it delivers an excellent Strehl ratio (better than 0.353) in the entire imaging FOV up to 60″.

Again, the TAO performance can be further improved by conjugating the DM to the best-conjugated height. Table 6 and Fig. 4 show the results of the numerical simulation for the 1.65 μm wavelength, with the DM conjugated to the 1000 m best-conjugated height. Again, the best-conjugated

Table 5. Strehl Ratios with Different FOVs at 1.65 μm Wavelength and Zero Conjugated Height[a]

Imaging FOV	0″	12″	24″	36″	48″	60″	72″	84″	96″	108″	120″
SR: CAO	0.977	0.730	0.480	0.330	0.243	0.189	0.155	0.133	0.119	0.106	0.095
SR: 30″ OFOV	0.822	0.741	0.612	0.470	0.349	0.275	0.224	0.186	0.161	0.140	0.125
SR: 60″ OFOV	0.635	0.605	0.564	0.505	0.423	0.353	0.293	0.243	0.207	0.178	0.157
SR: 120″ OFOV	0.426	0.416	0.408	0.394	0.369	0.344	0.319	0.288	0.261	0.233	0.209

[a]Four guide stars are used.

Imaging FOV	0″	12″	24″	36″	48″	60″	72″	84″	96″	108″	120″
SR: CAO	0.977	0.730	0.480	0.330	0.243	0.189	0.155	0.133	0.119	0.106	0.095
SR: 30″ OFOV	0.864	0.790	0.678	0.553	0.431	0.348	0.289	0.243	0.208	0.182	0.158
SR: 60″ OFOV	0.717	0.680	0.639	0.586	0.503	0.429	0.363	0.305	0.260	0.223	0.193
SR: 120″ OFOV	0.522	0.512	0.500	0.485	0.454	0.424	0.392	0.353	0.318	0.282	0.249

[a]Four guide stars are used.

approach provides a significant improvement for the Strehl ratio for the on-axis and off-axis positions in the imaging FOV for that with a large OFOV. The TAOs with a OFOV from 30″ to 120″ all deliver good performance over the entire 60″ imaging FOV, while the 120″ OFOV delivers excellent overall Strehl ratio in the entire 120″ imaging FOV (with a Strehl ratio better than 0.249 over the entire imaging FOV).

Since the TAO is optimized for the minimum residual phase variance of the guide stars, to evaluate the TAO gain, we propose a merit function (MF), which is the ratio of the CAO phase variance to that of the TAO in the same guide star FOV positions,

$$\mathrm{MF} \frac{\sum_i^N (\sigma_i')^2}{\sum_i^N (\sigma_i)^2}, \qquad (8)$$

where N is the number of total guide stars, and it is 4 for our case. i is the index of the ith guide star. $(\sigma_i)^2$ is the residual phase variance of the ith guide star of the TAO. $(\sigma_i')^2$ is the residual phase variance of the ith guide star of the CAO. Of course, for a CAO, the WFS only uses the on-axis guide star that is located at the center of the FOV (see Fig. 1). However, the residual wave-front error for the other three guide stars in the wave-front sensing FOV can be calculated for the CAO. Since the four guide stars are uniformly located in the FOV and are used for the TAO optimization, which optimizes for the minimum residual phase variance of all four of these guide stars, they can be used to evaluate the TAO performance gain, by comparison to the corresponding

residual phase variance in the CAO. The residual phase variance $(\sigma)^2$ of each guide star is related to the Strehl ratio as $\mathrm{SR} = e^{-\sigma^2}$. Using the defined MF, we calculate the TAO gain with the data from Tables 4 (J band) and 6 (H band), with results listed in Table 7. Compared with the CAO, the TAO provides a gain between 1.31 and 1.75, depending on the OFOV size. The reduction of the residual phase variance over the OFOV implies that the tomographic wave-front information indeed provides a performance improvement for the TAO. For the same OFOV, the gain is almost identical for the J and H bands. It is clear that the TAOs with an OFOV of 30″ and 60″ deliver almost the same gain, while the gain for the 120″ OFOV is reduced, indicating that an OFOV with a size between 30″ and 60″ is a good choice.

D. Performance at Bad Seeing Condition

It is interesting to see the TAO's performance at different seeing conditions. The seeing condition is generally bad in the winter. Using the seeing profile from Table 1, we also calculate the TAO Strehl ratios at the bad seeing condition with a Fried parameter and an isoplanatic angle of 5.5 cm and 2″, respectively. The Strehl ratios of the TAO at the 1.25 μm J band are shown in Table 8, in which the DM is conjugated at the best-conjugated height of 800 m. Again, the Strehl ratios of the CAO are also shown for comparison. The TAOs with OFOVs of 30″ and 60″ can deliver a Strehl ratio ~0.2 at 24″ imaging FOV, which is lower than that at the average seeing condition, but is still much better than the 0.117
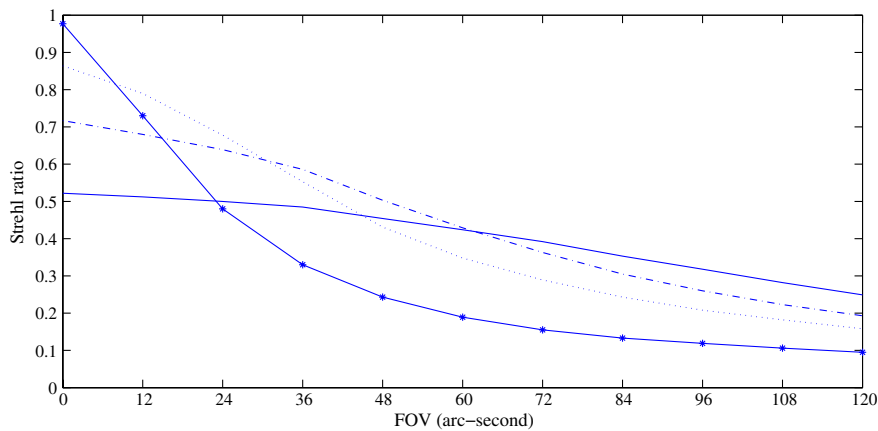
Fig. 4. Strehl ratios with different OFOVs with DM conjugated to 1.0 km height at 1.65 μm NIR. The solid line with star markers represents the CAO; dotted line, optimized for 30″ OFOV; dash dotted line, optimized for 60″ OFOV; solid line without marker, optimized for 120″ OFOV.

Table 7. TAO Gains at the J (without Bracket) and H (in Bracket) Bands

OFOV	30″	60″	120″
MF	1.66 (1.69)	1.61 (1.75)	1.31 (1.47)

Strehl ratio of the CAO at the same imaging FOV. The TAO with the 120″ OFOV delivers further lower Strehl ratios and is not recommended for the TAO wave-front sensing, although it delivers a relatively uniform Strehl ratio over the entire 48″ image FOV.

As estimated, Strehl ratios are better at longer wavelengths. Table 9 shows the Strehl ratios of the TAO at the 1.65 μm H band. Again, the DM is conjugated at the best-conjugated height, and the Strehl ratios of the CAO are also shown for comparison. Now, the TAO with the 30″ OFOV delivers a Strehl ratio ~0.201 at the 48″ imaging FOV, and the TAO with the 60″ OFOV delivers a Strehl ratio ~0.222 at the 60″ imaging FOV. The TAO with the 120″ OFOV still delivers a lower, but uniform, Strehl ratio over the entire 60″ image FOV. In a summary from Tables 8 and 9, both 30″ and 60″ OFOVs are optimal solutions for the TAO wave-front sensing.

Because of the bad seeing condition in the winter, the TAO delivers worse performance than that in the average seeing condition. Nevertheless, it is still able to deliver a Strehl ratio better than 0.22 over the entire imaging FOV 60″ in the 1.65 μm H band, and a Strehl ratio better than 0.20 over the entire imaging FOV 24″ in the 1.25 μm J band, which is much better than the CAO for large FOV imaging.

E. Performance at Good Seeing Condition

In the summer, good seeing is available. Again, using the seeing profile from the Table 1, we calculated the TAO Strehl ratios at the good seeing condition with a Fried parameter and an isoplanatic angle of 9.1 cm and 6″, respectively. The Strehl ratio of the TAO at the 1.25 μm J band is shown in Table 10, in which the DM is conjugated at the best-conjugated height of 900 m. The TAOs with OFOVs of 30″, 60″, and 120″ all deliver a Strehl ratio better than 0.291 at the 60″ imaging FOV, which is much better than that at the average seeing condition. Now, the TAO with the 120″ OFOV delivers overall good performance over the entire 120″ imaging FOV.

If we move to the longer wavelength 1.65 μm H band, the TAO delivers excellent performance for all OFOVs in the imaging FOV up to 120″, as shown in Table 11. Now, even the CAO delivers good performance for an imaging FOV up to 60″. In fact, because of the good seeing and large isoplanatic angle, the TAO can deliver good performance at any conjugated height between 0 and 900 mm.

F. Performance with Future 4 m Telescopes

Until now, we have evaluated the TAO performance with a 1.6 m telescope. Future solar telescopes should have an aperture diameter up to 4 m. For such a large aperture, it will be a great challenge to correct the atmospheric turbulence over a large FOV in the

Table 8. Strehl Ratios with Different OFOVs at 1.25 μm Wavelength and 800 m Conjugated Height[a]

Imaging FOV	0″	12″	24″	36″	48″	60″	72″	84″	96″	108″	120″
SR: CAO	0.941	0.343	0.117	0.064	0.045	0.035	0.029	0.026	0.024	0.022	0.021
SR: 30″ OFOV	0.510	0.364	0.233	0.147	0.090	0.067	0.054	0.045	0.039	0.035	0.032
SR: 60″ OFOV	0.247	0.214	0.192	0.170	0.126	0.100	0.081	0.064	0.055	0.047	0.041
SR: 120″ OFOV	0.127	0.119	0.117	0.116	0.105	0.098	0.091	0.080	0.073	0.063	0.056

[a]Four guide stars are used.

Table 9. Strehl Ratios with Different OFOVs at 1.65 μm Wavelength and 800 m Conjugated Height[a]

Imaging FOV	0″	12″	24″	36″	48″	60″	72″	84″	96″	108″	120″
SR: CAO	0.966	0.535	0.261	0.158	0.114	0.090	0.076	0.067	0.062	0.059	0.057
SR: 30″ OFOV	0.677	0.554	0.413	0.294	0.201	0.167	0.131	0.112	0.100	0.091	0.083
SR: 60″ OFOV	0.430	0.394	0.365	0.332	0.268	0.222	0.187	0.156	0.136	0.119	0.106
SR: 120″ OFOV	0.269	0.259	0.256	0.254	0.237	0.224	0.212	0.191	0.176	0.155	0.140

[a]Four guide stars are used.

Table 10. Strehl Ratios with Different OFOVs at 1.25 μm Wavelength and 900 m Conjugated Height[a]

Imaging FOV	0″	12″	24″	36″	48″	60″	72″	84″	96″	108″	120″
SR: CAO	0.974	0.629	0.370	0.251	0.192	0.158	0.137	0.125	0.120	0.114	0.108
SR: 30″ OFOV	0.779	0.687	0.571	0.455	0.348	0.291	0.254	0.225	0.208	0.193	0.181
SR: 60″ OFOV	0.591	0.559	0.533	0.501	0.434	0.382	0.338	0.294	0.265	0.237	0.216
SR: 120″ OFOV	0.446	0.443	0.431	0.428	0.406	0.391	0.373	0.344	0.322	0.291	0.266

[a]Four guide stars are used.

Table 11. Strehl Ratios with Different OFOVs at 1.65 μm Wavelength and 900 m Conjugated Height[a]

Imaging FOV	0″	12″	24″	36″	48″	60″	72″	84″	96″	108″	120″
SR: CAO	0.985	0.765	0.554	0.429	0.355	0.309	0.279	0.262	0.257	0.249	0.241
SR: 30″ OFOV	0.866	0.805	0.720	0.625	0.527	0.467	0.427	0.395	0.376	0.359	0.346
SR: 60″ OFOV	0.736	0.712	0.692	0.666	0.610	0.562	0.519	0.475	0.444	0.414	0.389
SR: 120″ OFOV	0.620	0.609	0.607	0.605	0.586	0.573	0.556	0.530	0.507	0.475	0.448

[a]Four guide stars are used.

Table 12. Strehl Ratios with Different OFOVs at 1.25 μm Wavelength and 1000 m Conjugated Height[a]

Imaging FOV	0″	12″	24″	36″	48″	60″	72″	84″	96″	108″	120″
SR: CAO	0.960	0.540	0.221	0.099	0.054	0.034	0.025	0.020	0.017	0.015	0.013
SR: 30″ OFOV	0.761	0.628	0.440	0.277	0.163	0.105	0.073	0.054	0.041	0.033	0.026
SR: 60″ OFOV	0.493	0.451	0.391	0.319	0.230	0.164	0.117	0.083	0.061	0.047	0.036
SR: 120″ OFOV	0.253	0.243	0.231	0.216	0.189	0.164	0.138	0.112	0.090	0.071	0.056

[a]Four guide stars are used.

visible with a MCAO that will need several DMs. It will be interesting to investigate the TAO performance in the NIR with such a large solar telescope.

Using the seeing data at the average seeing condition from Table 1, we have conducted the estimated TAO performance at the 1.25 μm J band at the best-conjugated height. This is achieved by simply changing the telescope aperture from 1.6 to 4 m. Table 12 shows the Strehl ratios at 1.25 μm. Comparing Tables 4 and 12, it is clear that the performance of both TAO and CAO is degraded with the 4 m telescope, because of the large aperture size. Now, the 60″ OFOV still delivers the best overall performance with a Strehl ratio of 0.23 at 48″ imaging FOV, compared with the Strehl ratio of 0.054 for the CAO at the same FOV position.

The estimated performance at the 1.65 μm H band is shown in Table 13. At the 60″ OFOV, the TAO delivers a Strehl ratio better than 0.339 over the entire 60″ imaging FOV. In fact, due to the longer wavelength, the TAO delivers good performance with an OFOV between 30″ and 60″, while the 60″ OFOV is still the best, in terms of the overall performance over the 60″ imaging FOV.

4. Discussion

The simulations we conducted until now are based on star-oriented tomographic wave-font reconstruction, in which several guide stars are used for tomographic wave-front sensing. Current nighttime MCAO techniques can be divided into two categories:

star-oriented (SO) [52] and layer-oriented (LO) [53] systems, both using several guide stars and several DMs for tomographic wave-front sensing and correction, respectively. For a nighttime MCAO system, several S-H WFSs are needed, each for one guide star. The GLAO concept has been proposed as a solution for improving uniformly the quality of wide-field images, typically 10 arc min [54], in which several guide stars and thus several WFSs are used. For this reason, GLAO systems aim at compensating for the boundary layer of the atmosphere, which is at the same time the location of most of the atmospheric turbulence and the layer for which correction remains valid on a wide FOV. Because of the extreme low SRs, the performance of GLAO is typically evaluated by the full width at half-maximum (FWHM) of the PSF, and accordingly GLAO is used only as a seeing improvement technique [55,39]. The GLAO can be viewed as the simplest of the LO MCAO systems, since only one DM is used. In GLAO, WFSs are conjugated to the ground and the wave-front sensing is done by simply averaging all wave-fronts from all guide stars [54]. Current solar GLAO, which targets for the seeing improvement over a large FOV, requires a WFS FOV larger than several arc minutes in diameter, which is not implementable at least based on the current technique, because of the challenge of wave-front sensing over such a large FOV [9]. As a result, solar GLAO has not been demonstrated in practice. Our TAO uses the same technique with the star-oriented MCAO, except only

Table 13. Strehl Ratios with Different OFOVs at 1.65 μm Wavelength and 1000 m Conjugated Height[a]

Imaging FOV	0″	12″	24″	36″	48″	60″	72″	84″	96″	108″	120″
SR: CAO	0.977	0.701	0.413	0.246	0.159	0.112	0.085	0.069	0.060	0.051	0.044
SR: 30″ OFOV	0.858	0.765	0.620	0.468	0.335	0.251	0.196	0.157	0.129	0.109	0.091
SR: 60″ OFOV	0.664	0.630	0.579	0.512	0.420	0.339	0.272	0.216	0.174	0.142	0.117
SR: 120″ OFOV	0.446	0.437	0.423	0.406	0.374	0.342	0.306	0.267	0.231	0.195	0.164

[a]Four guide stars are used.

one DM is used. Another significant difference among the TAO, nighttime LO GLAO, and MCAO is that the TAO only needs one WFS, in which all guide stars can be imaged in each WFS subaperture.

In order to define the conditions in which the LO approach is equivalent to other linear reconstruction schemes, a simplified analysis was conducted by Diolaiti *et al.* [56]. It is found that this approach is equivalent to an optimum one, under certain assumptions. That is, if the FOV weighting function is a sum of delta functions, one for each guide star, the correction is optimal: in this case the LO approach coincides with the SO classical one. If this is the case, the simulations of our TAO can also be applied to a solar LO AO system, in which only one WFS and one guide star are needed. In this scenario, a FOV with a size of ~40″ × 40″ will be used as a guide star for the solar LO AO system, and no tomographic wave-front reconstruction is needed; a solar CAO can be used for this purpose, without any change, and the wave-front sensing in the 40″ × 40″ FOV is done by the solar cross correlation, which automatically finds the WFS slope vectors for the AO correction loop. Since such a large WFS FOV is needed, the WFS CMOS camera can only sample the FOV at a low sampling scale, such as 1″/pixel, which requires that cross-correlation calculation must be able to provide subpixel accuracy—a technique that was demonstrated by our recent experiences [57,58]. This will dramatically simplify the development of a solar high-angular solution imaging system over a large FOV up to 60″ × 60″ in the NIR. The results of our recent LO solar AO experiences [57,58], which used a WFS FOV of 30″ × 30″ and showed good correction in the NIR and not the visible, are in good agreement with the TAO simulations discussed in this paper.

Current BBSO site test using the S-DIMM+ technique can only deliver four layers of the turbulence profile. Further increasing the measured height resolution is critical not only for the TAO, but also for MCAO systems with future 4 m solar telescopes that may need up to 5 DMs [13]. A technique called slope detection and ranging (SLODAR) that uses S-H WFSs to measure the turbulence profile was proposed for nighttime astronomy in the past [59,60]. This technique has reached a degree of maturity exhibiting reasonable agreement when used together in campaigns ([61], Cerro Tololo campaign). Recently, an improved version called generalized SLODAR was presented by Goodwin *et al.* [62], which can provide an improvement on the nominal height resolution by a factor of 3, and is a potential technique for future solar turbulence profile measurement with high precision.

5. Conclusions

We proposed a solar TAO system, which uses only one DM and fully takes advantage of the three-dimensional wave-front information measured by the WFS. Based on the recent site seeing test on the BBSO, we generated turbulence profiles that can be used for TAO performance simulations. Our numerical simulations showed that the TAO cannot deliver acceptable performance over a large imaging FOV in the 0.55 μm visible, since the residual wave-front error is still too large. However, the one-DM TAO can deliver good performance in wavelengths in the NIR J and H bands. We showed that there is a best-conjugated height where most of the turbulence is concentrated and can be effectively corrected, if the DM is optically conjugated to that altitude. At the best-conjugated height, the TAO performance can be further improved over a large FOV. In the average seeing condition, the TAO can provide good performance in the NIR for an imaging FOV up to 60″. We also showed that the best DM conjugated height can be found by numerical simulation. We demonstrated that a wave-front sensing OFOV between 30″ and 60″ is beneficial to the TAO for high-resolution imaging over a large imaging FOV on the order of 60″. Since only one DM is needed, the TAO is simple to implement. By simply replacing the WFS, an existing solar adaptive optics system can be adopted as a TAO system, and can be used for high-spatial-resolution and highly sensitive magnetic investigations in the NIR over a large FOV.

References and Notes

1. J. M. Beckers, "Increasing the size of the isoplanatic patch with multi-conjugate adaptive optics," in *Proceedings of European Southern Observatory Conference and Workshop on Very Large Telescopes and Their Instrumentation*, M. H. Ulrich, ed., Vol. **30** of ESO Conference and Workshop Proceedings (European Southern Observatory, 1988), pp. 693–703.
2. D. C. Johnston and B. M. Welsh, "Analysis of multi-conjugate adaptive optics," J. Opt. Soc. Am. A **11**, 394–408 (1994).
3. R. Ragazzoni, E. Marchetti, and F. Rigaut, "Modal tomography for adaptive optics," Astron. Astrophys. **342**, L53–L56 (1999).
4. A. Tokovinin and E. J. Viard, "Limiting precision of tomographic phase estimation," J. Opt. Soc. Am. A **A18**, 873–882 (2001).
5. B. L. Ellerbroek, L. Gilles, and C. R. Vogel, "Numerical simulations of multi-conjugate adaptive optics wave-front reconstruction on giant telescope," Appl. Opt. **42**, 4811–4818 (2003).
6. F. Rigaut, B. Neichel, M. Boccas, C. d'Orgeville, G. Arriagada, V. Fesquet, S. J. Diggs, C. Marchant, G. Gausach, W. N. Rambold, J. Luhrs, S. Walker, E. R. Carrasco-Damele, M. L. Edwards, P. Pessev, R. L. Galvez, T. B. Vucina, C. Araya, A. Gutierrez, A. W. Ebbers, A. Serio, C. Moreno, C. Urrutia, R. Rogers, R. Rojas, C. Trujillo, B. Miller, D. A. Simons, A. Lopez, V. Montes, H. Diaz, F. Daruich, F. Colazo, M. Bec, G. Trancho, M. Sheehan, P. McGregor, P. J. Young, M. C. Doolan, J. van Harmelen, B. L. Ellerbroek, D. Gratadour, and A. Garcia-Rissmann, "GeMS: first on-sky results," Proc. SPIE **8447**, 84470I (2012).
7. R. Ragazzoni, J. Farinato, and E. Marchetti, "Adaptive optics for 100 m class telescopes: new challenges require new solutions," Proc. SPIE **4007**, 1076–1087 (2000).

8. T. R. Rimmele, F. Woeger, J. Marino, K. Richards, S. Hegwer, T. Berkefeld, D. Soltau, D. Schmidt, and T. Waldmann, "Solar multi-conjugate adaptive optics at the Dunn Solar Telescope," Proc. SPIE **7736**, 773631 (2010).

9. A. Kellerer, "Layer-oriented adaptive optics for solar telescopes," Appl. Opt. **51**, 5743–5751 (2012).

10. T. R. Rimmele, K. Richards, J. Roche, S. Hegwer, and A. Tritschler, "Progress with solar multi-conjugate adaptive optics at NSO," Proc. SPIE **6272**, 627206 (2006).

11. T. Berkefeld, D. Soltau, and O. von der Lühe, "Multi-conjugate solar adaptive optics with the VTT and GREGOR," Proc. SPIE **6272**, 627205 (2006).

12. T. R. Rimmele and J. Marino, "Solar adaptive optics," Living Rev. Solar Phys. **8**, 2–92 (2011).

13. T. Berkefeld and D. Soltau, "EST adaptive optics performance estimations," Astron. Nachr. **331**, 640–643 (2010).

14. T. Fusco, S. Meimon, Y. Clenet, M. Cohen, H. Schnetler, J. Paufique, V. Michau, J.-P. Amans, D. Gratadour, C. Petit, C. Robert, P. Jagourel, E. Gendron, G. Rousset, J.-M. Conan, and N. Hubin, "ATLAS: the E-ELT laser tomographic adaptive optics system," Proc. SPIE **7736**, 773601 (2010).

15. T. Berkefeld, personal communication, 2013.

16. E. J. Seykora, "Solar scintillation and the monitoring of solar seeing," Sol. Phys. **145**, 389–397 (1993).

17. J. M. Beckers, "On the relation between scintillation and seeing observations of extended objects," Sol. Phys. **145**, 399–402 (1993).

18. J. M. Beckers, "Daytime seeing measurements for the advanced technology Solar telescope," in *Astronomical Site Evaluation in the Visible and Radio Range. ASP Conference Proceedings*, J. Vernin, Z. Benkhaldoun, and C. Muñoz-Tuñón, eds. (Astronomical Society of the Pacific, 2002), Vol. **266**, pp. 350–357.

19. G. B. Scharmer and T. I. M. van Werkhoven, "S-DIMM+ height characterization of day-time seeing using solar granulation," Astron. Astrophys. **513**, A25 (2010).

20. A. Kellerer, N. Gorceix, J. Marino, W. Cao, and P. R. Goode, "Profiles of the daytime atmospheric turbulence above Big Bear solar observatory," Astron. Astrophys. **542**, A2 (2012).

21. A. Kellerer, personal communication, 2013.

22. F. Hill, R. Radick, and M. Collados, "Deriving $C_n^2(h)$ from a scintillometer array, project documentation," ATST Report #0014, Revision A (2003), p. 18.

23. D. L. Fried, "Statistics of a geometric representation of wavefront distortion," J. Opt. Soc. Am. **55**, 1427–1431 (1965).

24. H. Socas-Navarro, J. Beckers, P. Brandt, J. Briggs, T. Brown, W. Brown, M. Collados, C. Denkere, S. Fletcher, S. Hegwer, F. Hill, T. Horst, M. Komsa, J. Kuhn, A. Lecinski, H. Lin, S. Oncley, M. Penn, T. Rimmele, and K. Streander, "Solar site survey for the advanced technology solar telescope. I. Analysis of the seeing data," Publ. Astron. Soc. Pac. **117**, 1296–1305 (2005).

25. F. Roddier, "The effect of atmospheric turbulence in optical astronomy," in *Progress in Optics XIX*, E. Wolf, ed. (North Holland, 1981), pp. 281–376.

26. R. K. Tyson, "Adaptive optics and ground-to-space laser communications," Appl. Opt. **35**, 3640–3646 (1996).

27. R. K. Tyson, *Principles of Adaptive Optics*, 3rd ed. (CRC Press, 2011), Chap. 2, p. 28.

28. B. L. Ellerbroek, "Wavefront reconstruction algorithms and simulation results for multiconjugate adaptive optics on giant telescopes," Proc. SPIE **5382**, 478–489 (2004).

29. A. Tokovinin and M. Le Louarn, "Isoplanatism in a multiconjugate adaptive optics system," J. Opt. Soc. Am. A **17**, 1819–1827 (2000).

30. T. Fusco, J. M. Conan, G. Rousset, L. M. Mugnier, and V. Michau, "Optimal wave-front reconstruction strategies for multiconjugate adaptive optics," J. Opt. Soc. Am. A **18**, 2527–2538 (2001).

31. A. Tokovinin and E. Viard, "Limiting precision of tomographic phase estimation," J. Opt. Soc. Am. A **18**, 873–882 (2001).

32. B. Dong, D. Ren, and X. Zhang, "Numerical analysis of modal tomography for solar multi-conjugate adaptive optics," Res. Astron. Astrophys. **12**, 465–471 (2012).

33. B. L. Ellerbroek, "First-order performance evaluation of adaptive-optics systems for atmospheric-turbulence compensation in extended-field-of-view astronomical telescopes," J. Opt. Soc. Am. A **11**, 783–805 (1994).

34. T. Fusco, J.-M. Conan, V. Michau, L. M. Mugnier, and G. Rousset, "Phase estimation for large field of view: application to multi-conjugate adaptive optics," Proc. SPIE **3763**, 125–133 (1999).

35. B. Femenía and N. Devaney, "Optimization with numerical simulations of the conjugate altitudes of deformable mirrors in an MCAO system," Astron. Astrophys. **404**, 1165–1176 (2003).

36. D. T. Gavel, "Tomography for multi-conjugate adaptive optics systems using laser guide stars," Proc. SPIE **5490**, 1356–1373 (2004).

37. D. R. Andersen, J. Stoesz, S. Morris, M. Lloyd-Hart, D. Crampton, T. Butterley, B. Ellerbroek, L. Jolissaint, N. M. Milton, R. Myers, K. Szeto, A. Tokovinin, J. P. Véran, and R. Wilson, "Performance modeling of a wide-field ground-layer adaptive optics system," Publ. Astron. Soc. Pac. **118**, 1574–1590 (2006).

38. B. L. Ellerbroek, "Linear systems modeling of adaptive optics in the spatial-frequency domain," J. Opt. Soc. Am. A **22**, 310–322 (2005).

39. A. Tokovinin, "Seeing improvement with ground-layer adaptive optics," Publ. Astron. Soc. Pac. **116**, 941–951 (2004).

40. M. Lloyd-Hart and N. M. Milton, "Multi-conjugate adaptive optics for a new generation of giant telescopes," Proc. SPIE **4840**, 18–26 (2003).

41. A. G. Basden, T. Butterley, R. M. Myers, and R. W. Wilson, "Durham extremely large telescope adaptive optics simulation platform," Appl. Opt. **46**, 1089–1098 (2007).

42. B. L. Ellerbroek, "Adaptive optics without borders: performance evaluation in the infinite aperture limit," Proc. SPIE **5490**, 625–636 (2004).

43. J. X. Cheng, M. D. Ding, and J. P. Li, "Diagnostics of the heating processes in solar flares using chromospheric spectral lines," Astrophys. J. **653**, 733–738 (2006).

44. R. J. Rutten, "Observing the solar chromosphere," in *The Physics of Chromosphere Plasmas*, P. Heinzel, I. Dorotovic, and R. J. Rutten, eds., Vol. **268**, ASP Conference Series (Astronomical Society of the Pacific, 2007), pp. 27–48.

45. G. Cauzzi, K. P. Reardon, H. Uitenbroek, F. Cavallini, A. Falchi, R. Falciani, K. Janssen, T. Rimmele, A. Vecchio, and F. Wöger, "The solar chromosphere at high resolution with IBIS. I. New insights from the Ca II 854.2 nm line," Astron. Astrophys. **480**, 515–526 (2008).

46. U. Grossmann-Doerth, C. U. Keller, and M. Schüssler, "Observations of the quiet Sun magnetic field," Astron. Astrophys., **315**, 610–617 (1996).

47. H. Socas-Navarro and J. Sánchez Almeida, "Magnetic properties of photospheric regions with very low magnetic flux," Astrophys. J. **565**, 1323–1334 (2002).

48. H. Lin and T. Rimmele, "The granular magnetic fields of the quiet sun," Astrophys. J. **514**, 448–455 (1999).

49. W. V. Khomenko, M. Collados, S. K. Solanki, A. Lagg, and J. Trujillo-Bueno, "Quiet-Sun inter-network magnetic fields observed in the infrared," Astron. Astrophys. **408**, 1115–1135 (2003).

50. J. Ramsauer, S. K. Solanki, and E. Biémont, "Interesting lines in the infrared solar spectrum. II. Unblended lines between λ 1.0 and λ 1.8 um," A&AS **113**, 71–89 (1995).

51. J. W. Hardy, *Adaptive Optics for Astronomical Telescope* (Oxford University, 1998), Chap. 3, p 103.

52. J. M. Beckers, "Increasing the size of the isoplanatic patch with multiconjugate adaptive optics," in *ESO Conference and Workshop Proceedings on Very Large Telescopes and Their Instrumentation* (European Southern Observatory, 1988), p. 693–703.

53. R. Raggazzoni, E. Dialaiti, J. Farinato, E. Fedrigo, E. Marchetti, M. Tordi, and D. Kirkman, "Multiple field of view layer-oriented adaptive optics. Nearly whole sky coverage on 8 m class and beyond," Astron. Astrophys. **396**, 731–744 (2002).

54. M. Nicolle, T. Fusco, V. Michau, G. Rousset, and J. L. Beuzit, "Optimization of star-oriented and layer-oriented wavefront sensing concepts for ground layer adaptive optics," J. Opt. Soc. Am. A **23**, 2233–2245 (2006).

55. M. Hart, N. M. Milton, C. Baranec, K. Powell, T. Stalcup, D. McCarthy, C. Kulesa, and E. Bendek, "A ground-layer adaptive optics system with multiple laser guide stars," Nature **466**, 727–729 (2010).

56. E. Diolaiti, R. Ragazzoni, and M. Tordi, "Closed loop performance of a layer-oriented multi-conjugate adaptive optics system," Astron. Astrophys. **372**, 710–718 (2001).

57. D. Ren and Y. Zhu, "A solar adaptive optics system," in *Adaptive Optics Progress*, R. K. Tyson, ed. (InTech, 2013), Chap. 2, pp. 22–40.

58. D. Ren, R. Li, X. Zhang, J. Dou, Y. Zhu, and G. Zhao, "The first portable solar and stellar adaptive optics," Proc. SPIE (submitted).

59. R. W. Wilson, "SLODAR: measuring optical turbulence altitude with a Shack–Hartmann wavefront sensor," Mon. Not. R. Astron. Soc. **337**, 103–108 (2002).

60. T. Butterley, R. W. Wilson, and M. Sarazin, "Determination of the profile of atmospheric optical turbulence strength from SLODAR data," Mon. Not. R. Astron. Soc. **369**, 835–845 (2006).

61. A. Tokovinin and T. Travouillon, "Model of optical turbulence profile at Cerro Pachón," Mon. Not. R. Astron. Soc. **365**, 1235–1242 (2006).

62. M. Goodwin, C. Jenkins, and A. Lambert, "Improved detection of atmospheric turbulence with SLODAR," Opt. Express **15**, 14844–14860 (2007).